Enhancement of thermoelectric efficiency of T-$HfSe_2$ via nanostructuring

E. Unsal [1,2] R. T. Senger [1,3] and H. Sevinçli [2,*]

[1]*Department of Physics, Izmir Institute of Technology, 35430 Izmir, Turkey*

[2]*Department of Materials Science and Engineering, Izmir Institute of Technology, 35430 Izmir, Turkey*

[3]*Department of Physics, University of California, Davis, California 95616, USA*

(Received 5 June 2020; revised 27 October 2020; accepted 8 December 2020; published 11 January 2021)

In this work, *ab initio* calculations based on density functional theory and the Landauer formalism are carried out to investigate ballistic thermoelectric properties of T-$HfSe_2$ nanoribbons (NRs). The zigzag-edged NRs are metallic, and they are not included in this study. The armchair NRs possess two types of edge symmetries depending on the number of atoms present in a row; odd-numbered NRs have mirror symmetry, whereas the even-numbered NRs have glide reflection symmetry. The armchair-edged NRs are dynamically stable and show semiconducting properties with varying band gap values in the infrared and visible regions. Detailed transport analyses show that the n-type Seebeck coefficient and the power factor differ because of the structural symmetry, whereas the p-type thermoelectric coefficients are not significantly influenced. It is shown that the phonon thermal conductance is reduced to a third of its two-dimensional value via nanostructuring. The p-type Seebeck coefficient and the power factor for T-phase $HfSe_2$ are enhanced in NRs. We report that the p-type ZT value of $HfSe_2$ NRs at 300 and 800 K are enhanced by factors of 4 and 3, respectively.

DOI: 10.1103/PhysRevB.103.014104

I. INTRODUCTION

Thermoelectric materials have been of great interest due to their ability of direct conversion between heat and electrical energies. A good thermoelectric system is pretty enduring and feasible for working in a wide temperature range, and it provides environment-friendly energy conversion efficiently [1,2]. The efficiency of a thermoelectric material is measured with a dimensionless figure of merit, $ZT = (\sigma S^2 T)/\kappa_{tot}$, where σ, S, and T are the electrical conductivity, Seebeck coefficient, and temperature, respectively [3]. κ_{tot} is the total thermal conductivity of the material, defined as the sum of the contributions from the charge carriers and the lattice vibrations. Based on this formula, an efficient thermoelectric material should have a high Seebeck coefficient and good electrical conductivity and low thermal conductivity simultaneously.

As coolers or power generators, these materials can be widely used in nanodevice applications in infrared sensors [4,5], computer chips [6,7], and satellites [8,9]. Applications of these materials are limited due to their low efficiency. For instance, commercially, typical ZT values are usually about 1, and the experimental values may reach up to around 3 [10–12]. Increasing the thermoelectric efficiency of materials has been an ambitious goal for decades. Accordingly, many strategies have been proposed to enhance the efficiency of thermoelectric materials.

The enhancement of the thermoelectric efficiency can be achieved by enhancing the Seebeck coefficient and the electrical conductivity of the material and by reducing the total thermal conductivity. However, it is challenging to achieve these simultaneously. According to Wiedemann-Franz law [13], the electrical and thermal conductivities are directly proportional, which means that reducing the thermal conductivity of electrons leads to a decrease in the electrical conductivity. Therefore, the so-called phonon-glass electron-crystal concept [14,15], which aims at maximizing S and σ while minimizing the phonon thermal conductivity, is usually applied for the ZT optimization [16]. In the selection of thermoelectric materials, a crystal that possesses the charge transport mechanism of a semiconductor with hindered lattice thermal conduction [17] is mostly preferred.

For manipulation of phonon thermal conductivity, reducing the dimension of materials (such as generating heterostructures, forming their nanoribbons or quantum dots) [18–20] is a commonly used method. Hicks and Dresselhaus theoretically showed that generating quantum well [21] and quantum wire [22] structures of bulk materials leads to significant changes in their ZT values due to the confined movements of the electrons. Moreover, dimension reduction also leads to suppression of phonon thermal conductivity due to the increased scatterings from the boundaries of the structures. Consequently, the ZT value is improved by decreasing the phonon thermal conductivity. Reducing the dimensionality of a system also leads to an increase in its Seebeck coefficient [23–25]. As the size of the material becomes smaller, there occurs qualitative changes in its electronic density of states (DOS) due to quantum confinement effects [26–28]. Distribution of the conducting channels and transmission spectrum, which play a crucial role in transport calculations, are closely related to the DOS [29,30]. Substantial changes in the transmission spectrum lead to an increase in S approximated as $S \approx (\pi^2 k_B^2 T/3e)[d\ln\tau(E)/dE]$ at low temperatures, where k_B

*haldunsevincli@iyte.edu.tr

is the Boltzmann constant, e is the electron charge, and $\tau(E)$ is the energy-dependent transmission function [31–33].

In this respect, two-dimensional (2D) transition metal dichalcogenides (TMDs) are promising thermoelectric materials [34–38] since they have low thermal conductivity, while they exhibit high electrical conductivity [39]. Moreover, their mechanical flexibility [40,41] and high chemical stability make their synthesis relatively easier. Among TMDs, Hf-based compounds have relatively high thermoelectric efficiencies [42–45]. The mainspring for their high thermoelectric efficiency is their low lattice thermal conductivity [46], which arises mainly from heavy Hf atoms and partly from the strong couplings between acoustic and low-frequency optical modes [47]. Recently, the 2D air-stable trigonal (T) phase of $HfSe_2$ was synthesized down to a three-layer thickness [48].

Herein, we study the enhancement in thermoelectric efficiency of T-$HfSe_2$ via nanostructuring. Nanoribbon structures of T-$HfSe_2$ are constructed with various widths. We investigate their structural, vibrational, and electronic properties by using density functional theory (DFT)-based *ab initio* calculations and their ballistic thermoelectric properties within the Landauer formalism.

This paper is organized as follows: Details of the computational methodology used are given in Sec. II. The structural, vibrational, and electronic properties of two-dimensional and nanoribbon structures of $HfSe_2$ are discussed in Sec. III in detail. Last, Sec. IV gives the conclusions.

II. METHODOLOGY

DFT-based calculations were performed by using the Vienna Ab initio Simulation Package (VASP) [49,50]. In order to describe the exchange-correlation functionals, we use the Perdew-Burke-Ernzerhof (PBE) [51] form of the generalized gradient approximation functional. The Heyd-Scuseria-Ernzerhof (HSE) approximation is included for the band gap estimation [52]. The Hartree-Fock mixing parameter is chosen to be 0.25.

The energy cutoff of the plane-wave basis set is chosen to be 250 eV. The energy difference between successive electronic steps is taken to be 10^{-5} eV. The Hellmann-Feynman forces on each atom are reduced to less than 10^{-4} eV/ Å. A vacuum space of 12 Å is incorporated for the confined directions (x and z directions). In geometric optimization calculations, $18 \times 18 \times 1$ and $1 \times 18 \times 1$ Γ-centered meshes are used for the Brillouin zone (BZ) integration for two-dimensional and nanoribbon structures, respectively.

The vibrational properties are investigated by using the small displacement method as implemented in PHONOPY code [53]. In phononic band spectrum calculations, a $1 \times 6 \times 1$ supercell was generated, and a $1 \times 10 \times 1$ Γ-centered mesh was used for the BZ integration.

Charge transport in the mesoscopic systems was examined successfully within the Landauer-Büttiker formalism [54–56]. The electrical conduction at nanoscales is characterized by the length scales of L and λ (the length of the material and the mean free path of the carriers, respectively) [57,58]. In the ballistic regime, L is much smaller than λ, and the scattering mechanisms which comprise scatterings from phonons, impurities, and defects can be ignored in this regime. Ballistic device approximation is commonly used in nanoscaled materials [59,60], especially for the nanoribbons [61,62] and nanotubes [63]. In the literature, ballistic transport in low-dimensional materials is observed in a wide range of device lengths (from 30 nm to 15 μm) [64–67]. By using the deformation potential theory [68] and the effective mass approximation [69], we estimate the electron mean free path in 2D $HfSe_2$ to be approximately 15 nm at room temperature. That figure sets up a natural upper bound for the size of the nanostructures where the ballistic transport approximation we employ remains valid.

Thermoelectric properties are investigated within the Landauer formalism. For the electronic part, we utilize the following equation [70]:

$$L_n = \frac{2}{h}\int_{-\infty}^{+\infty} d\varepsilon\tau(\varepsilon)\left(-\frac{\partial f(\varepsilon)}{\partial\varepsilon}\right)(\varepsilon-\mu)^n, \tag{1}$$

where $\partial f(\varepsilon)/\partial\varepsilon$ is the derivative of the Fermi distribution function. $\tau(\varepsilon)$ and μ are the energy ε dependent transmission function and the chemical potential, respectively. The electrical conductance G, Seebeck coefficient S, and the electronic thermal conductance κ_{el} can be expressed in terms of L_n integrals [71] as

$$G = e^2 L_0, \tag{2}$$

$$S = -\frac{L_1}{eTL_0}, \tag{3}$$

and

$$\kappa_{el} = \frac{1}{T}\left(L_2 - \frac{{L_1}^2}{L_0}\right). \tag{4}$$

Phonon thermal conductance can be described as [72,73]

$$\kappa_{ph} = \frac{1}{2\pi}\int_{-\infty}^{+\infty} dw\hbar\omega\tau(\omega)\frac{\partial f_{BE}(\omega,T)}{\partial T} \tag{5}$$

where f_{BE} is the Bose-Einstein distribution function, $f_{BE} = 1/[\exp(\hbar\omega/k_BT)-1]$, and $\tau(\omega)$ is the frequency ω dependent transmission function. In ballistic transport, the transmission function is calculated by counting the number of channels in the corresponding energy/frequency range.

By using the calculated coefficients, the dimensionless thermoelectric figure of merit ZT is obtained as follows:

$$ZT = \frac{S^2G}{\kappa_{el}+\kappa_{ph}}T, \tag{6}$$

where T is the temperature. Thermoelectric coefficients are calculated for the unit cell. Herein, there are several nanoribbons with different widths. In order to compare their electrical and thermal conductances with each other, the calculated values are scaled with respect to their width. Therefore, the given values are conductance per length.

III. RESULTS AND DISCUSSIONS

Ten different nanoribbon structures of $HfSe_2$ in the octahedral trigonal phase were analyzed. We consider only the nanoribbons (NRs) with armchair edges since the NRs with zigzag edges have metallic characteristics. The structural,

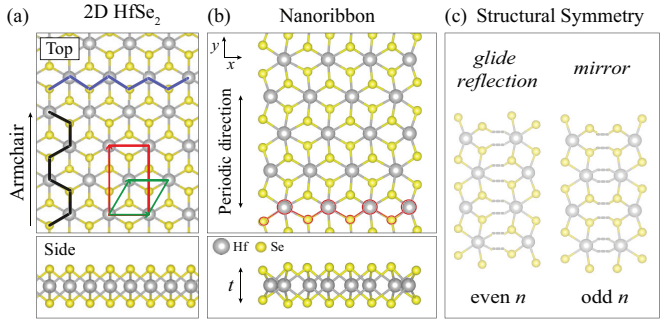

FIG. 1. The geometries of (a) 2D $HfSe_2$ and (b) its armchair nanoribbon (NR). Blue and black lines in (a) show the zigzag and armchair directions, respectively. The primitive and conventional unit cells are shown with the green rhombus and the red rectangle, respectively. The NRs are labeled according to the number of atoms n along their widths (highlighted with red circles). The NR in (b) has eight atoms along its width; thus, it is labeled as $n = 8$. (c) The symmetry of NR structures varies depending on whether n is odd or even: with regard to their edges, glide reflection (n even) and mirror symmetry (n odd).

vibrational, electronic, and thermoelectric properties will be discussed in detail separately.

A. Structural properties

The octahedral T phase of 2D $HfSe_2$ is formed with the arrangement of three atomic sublayers in the sequence of Se-Hf-Se. It belongs to the space group $P\bar{3}m1$ and the point group D_{3d}.

The optimized geometries of 2D $HfSe_2$ and its NR structures are shown in Fig. 1. The NRs are labeled with respect to their widths, with n denoting the number of atoms present in a zigzag chain along the transverse direction. As seen in Fig. 1(c), the edges of the NRs have two types of symmetry, glide reflection for even n and mirror for odd n.

For each NR, the calculated parameters such as the lattice constant (along the periodic direction), thickness, and width are given in Table I. As seen, the lattice constant b of NRs does not change significantly. The thickness is determined by measuring the vertical distance between the uppermost and lowermost Se atoms. Two-dimensional $HfSe_2$ has a thickness of 3.14 Å. The thickness of NRs increases about 4% with respect to the 2D $HfSe_2$, mainly at the edges. The average bond length in NRs is also examined, and it is found that it does not change drastically compared to the average bond length in the 2D $HfSe_2$.

TABLE I. The calculated parameters for the NR structures: the lattice constant along the periodic direction b, the thickness t, the width w, and the electronic band gap values calculated within PBE and PBE+HSE06 approximations, E_g^{PBE} and $E_g^{\mathrm{PBE+HSE06}}$, respectively.

NR	b (Å)	t (Å)	w (nm)	E_g^{PBE} (eV)	$E_g^{\mathrm{PBE+HSE06}}$ (eV)
$n = 6$	6.60	3.25	0.99	0.98	2.01
$n = 7$	6.53	3.27	1.18	0.67	1.37
$n = 8$	6.57	3.26	1.37	0.83	1.54
$n = 9$	6.54	3.26	1.56	0.68	1.37
$n = 10$	6.55	3.26	1.74	0.76	1.46
$n = 11$	6.54	3.26	1.93	0.67	1.36
$n = 12$	6.54	3.26	2.12	0.72	1.41
$n = 13$	6.54	3.26	2.30	0.66	1.35
$n = 14$	6.54	3.26	2.49	0.69	1.38
$n = 15$	6.53	3.26	2.68	0.66	1.34

B. Vibrational properties

We present the vibrational properties of 2D $HfSe_2$ and its NR structures in this part. The vibrational analyses show that each structure is dynamically stable since all phonon frequencies are positive throughout the BZ. The phonon band spectra of 2D $HfSe_2$ and its NR structures are given in Figs. 2(a) and 2(b), respectively. The phonon spectrum of 2D $HfSe_2$ is calculated for the primitive hexagonal unit cell, which consists of three atoms. Unit cells of NRs include between 18 and 45 atoms. There are $3N$ phonon branches in each spectrum, where N is the number of atoms in the unit cell.

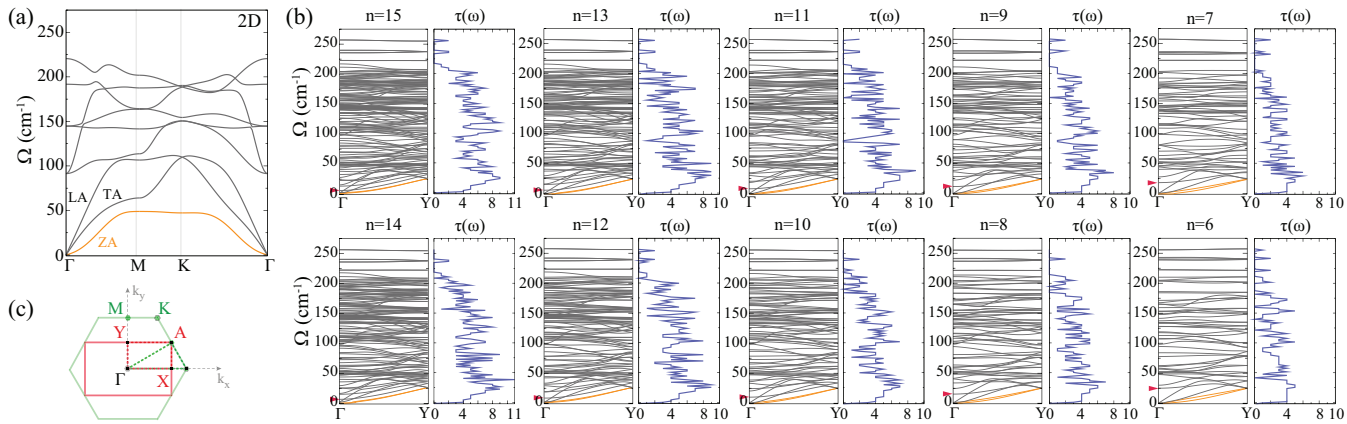

FIG. 2. The phonon band spectra of (a) 2D $HfSe_2$ and (b) its NRs. The NRs with odd and even n are shown in the first and second rows, respectively. Red triangles point out the optical phonon modes with the lowest frequencies. Twisting and out-of-plane acoustic modes are highlighted in orange. (c) Brillouin Zone folding.

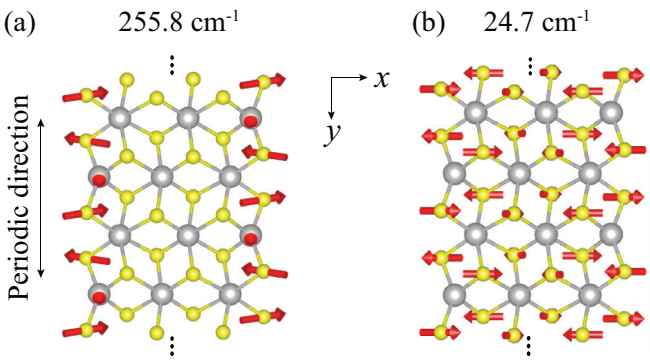

FIG. 3. Characters of optical phonon modes with (a) the highest and (b) the lowest frequencies are given for the NR with $n = 6$. The given frequency values are calculated at the Γ point.

For 2D structures, it is known that there are three acoustic phonon branches [including the in-plane transverse (T) and longitudinal (L) and the out-of-plane (Z) acoustic modes] and $3N - 3$ optical phonon branches. In one dimension, there is an additional acoustic mode, namely, the twisting (TW) mode, which is about the rotational motion, which costs zero energy ($\omega = 0$ at $k = 0$), around the central axis of a 1D system [74]. Reducing the dimension breaks the rotational symmetry and the degeneracy of the out-of-plane acoustic modes (ZA and TW), which causes the appearance of the TW mode [75]. For graphene nanoribbons, it is known that the ZA and TW modes become degenerate as the ribbon width gets wider [76,77]. As seen from Fig. 2(b), for the $HfSe_2$ NRs, two acoustic modes with the lowest frequencies (ZA and TW modes) become degenerate with increasing n.

Hf and Se are relatively heavy atoms, and therefore, the maximum frequency of the phonon branches has relatively lower values. As seen in Fig. 2(a), the maximum frequency of the optical phonon branch of 2D $HfSe_2$ is less than 225 cm^{-1} throughout the BZ. This value increases to greater than 250 cm^{-1} for each NR due the uncoordinated atoms at the ribbon edges. In the NR structures, the optical phonon modes with the highest frequency are edge-localized modes. As an example, one of these modes calculated for the NR with $n = 6$ is shown in Fig. 3(a), and its frequency is 255.8 cm^{-1} at the Γ point. As seen from Fig. 3, this mode is dominated by the motions of the edge atoms. These edge-localized modes reveal themselves as flat bands in the phonon band spectrum. Since these bands are dispersionless, their contribution to the transmission function can be missed. However, miscounting of these modes does not affect the thermoelectric property calculations since their contributions to the thermal conductance are weak.

In Fig. 2(b), the optical phonon modes with the lowest energy are highlighted with red triangles, and these modes can be used for the comparison of the width of NRs. The frequencies of these modes increase as the NR gets narrower. For the NR with $n = 6$, the frequency of that mode is 24.7 cm^{-1} at Γ, and its character is shown in Fig. 3(b).

C. Electronic properties

The electronic band structures of 2D $HfSe_2$ and its NRs calculated within the PBE are demonstrated in Figs. 4(b)–4(d). The 2D $HfSe_2$ is found to be a nonmagnetic semiconductor [42]. As their 2D counterpart, all armchair NRs of T-$HfSe_2$ have a semiconducting character. Within the PBE approximation, the calculated energy band gap is 0.6 eV for the 2D $HfSe_2$, and its estimated value is 1.5 eV with the HSE approximation. For the NRs, the energy band gap values calculated with PBE and their corrected values are given in Table I. The width dependency of the band gap obtained from PBE is given Fig. 4(a). The band gap values of NRs with odd n are almost the same, and they are about 600–700 meV higher than that of 2D $HfSe_2$. On the other hand, there is a notable difference for the energy band gaps of the NRs with even n. As the width of the NR structure increases, the band gap of the NRs converges to the 2D limit [see Fig. 4(a)].

As mentioned before, the NRs have periodicity along the y direction. For the sake of convenience in the comparison of the electronic structures of 2D $HfSe_2$ and its NRs, the electronic band spectrum is also calculated for the rectangular

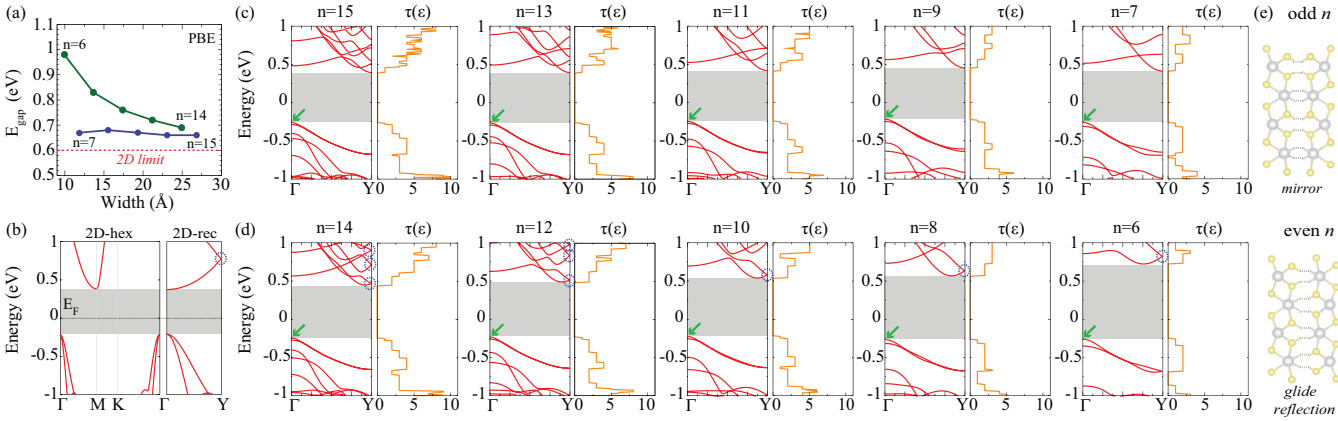

FIG. 4. (a) The width dependency of energy band gap values are represented. The 2D limit refers to the band gap value of 2D $HfSe_2$. The electronic band structures calculated within PBE are shown for (b) 2D $HfSe_2$ and its NR structures with (c) odd and (d) even n. The energy-dependent transmissions $\tau(\varepsilon)$ are also given for the NRs. The Fermi level E_F is set to zero in each band graph. Blue dashed circles and green arrows highlight the touching point of conduction bands and valence band convergence, respectively. (e) As a reminder, the symmetries of NRs with odd and even n are shown again.

unit cell of 2D $HfSe_2$, and it is given in Fig. 4(b). The folded band structure of the rectangular cell is shown only between the Γ- and Y-symmetry points in the BZ. In addition, for the 2D $HfSe_2$ with a hexagonal unit cell, there is a single conduction band in the 0–1-eV energy range of its electronic band structure. In the band structure of the rectangular unit cell of 2D $HfSe_2$, there are two conduction bands in the same energy range due to the folding of the BZ.

The band dispersion differs with respect to the structural symmetry of the NRs. The NRs with odd and even n have the same dispersion trend among themselves, and the dispersions of NRs with even n and 2D $HfSe_2$ are similar. The NR structures with even (odd) n are constructed by using an integer (fractional) number of 2D unit cells along the x axis (zigzag direction). Therefore, due to the zone folding, the band crossing (splitting) occurs at the zone edges for even (odd) n. A similar behavior was also reported for single-wall carbon nanotubes [74] and armchair graphene ribbons [78]. As seen in Figs. 4(b) and 4(d), the bands touch at the Y high-symmetry point, as highlighted with dashed blue circles. This is due to the fact that both 2D $HfSe_2$ and NRs with even n have the glide reflection symmetry.

For the NRs with odd n, the conduction bands are closer to being degenerate than they are in even n. The degenerate bands lead to an increment in transmission $\tau(\varepsilon)$. Degeneracy also causes a narrowing in the conduction plateaus and abrupt changes in the transmission. For the NRs with glide reflection symmetry (even n), as the ribbon width enlarges, the number of channels increases in the conduction part, and this results in an increment in transmission function. However, unlike the NRs with mirror symmetry (odd n), there are no abrupt changes in the transmission function, and the width of the conduction plateaus is relatively wider than that of NRs with odd n.

For valence bands of NRs with odd and even n, there is no sharp difference between their dispersions, so their transmissions are also similar. For each NR, the second valence band with the highest energy converges to the valence band with the maximum energy as the nanoribbon gets wider. The convergence is highlighted with the green arrows in Figs. 4(c) and 4(d). The valence band convergence leads to an increment in the transmission function which can be seen from the figure.

By definition, the effective mass m^* is calculated via $m^* = \hbar^2/(d^2E/dk^2)$ in the nearly-free-electron model where the bands are assumed to be parabolic. E is the k-dependent band energies attained from the numeric calculations, and the denominator of the equation, the second derivative of E with respect to k, is obtained by quadratic regression. The calculated effective masses of electrons m_e^* and holes m_h^* in 2D $HfSe_2$ and its NRs are given in Fig. 5. m_e^* and m_h^* values in the 2D structure are investigated along Γ-M, M-K, and Γ-Y. For the 2D structure, m_e^* is calculated to be 3.13 and 0.18 along Γ-M and M-K, respectively, which is consistent with the literature [47]. For 2D $HfSe_2$, the valence band maximum is degenerate at Γ. Our calculated m_h^* values are 0.12 and 0.33 along the Γ-M direction. Generally, there are no extreme differences in the effective mass values of NRs depending on whether the n is odd or even. As the width of the NR increases, the effective mass values get closer to the 2D limit.

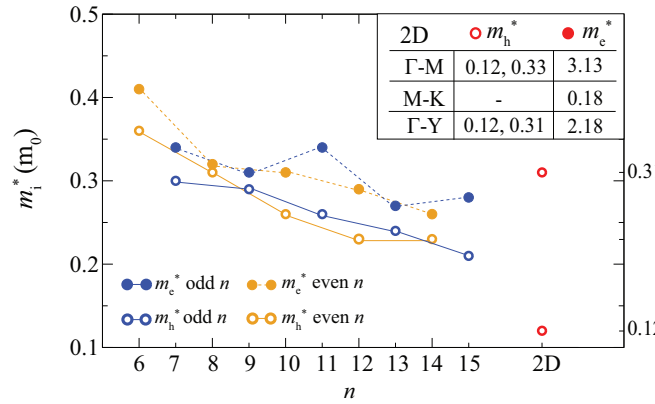

2D	m_h^*	m_e^*
Γ-M	0.12, 0.33	3.13
M-K	-	0.18
Γ-Y	0.12, 0.31	2.18

FIG. 5. The calculated effective mass values for 2D $HfSe_2$ and its NRs are given. The effective mass values m_i^* are given in terms of the free-electron mass m_0. The effective mass values are calculated along Γ-Y for NRs and along Γ-Y, Γ-M, and M-K for 2D $HfSe_2$.

D. Thermoelectric properties

In semiconducting materials, both electrons and holes contribute to the charge transport. In narrow-gap materials, the opposite contributions of holes and electrons can be simultaneous, and this results in suppression of the Seebeck coefficient. This suppression is negligible when the band gap is larger than $10k_BT$ [79]. Herein, the band gap values calculated via PBE are not narrower than $10k_BT$; thus, PBE results will be used for the thermoelectric parameter calculations. The spin-orbit coupling (SOC) is not included in this study since it is not expected to affect the results considerably. Our test calculations show that ZT is changed by less than 1% for $n = 6$ when SOC is included. At two different temperatures, the following thermoelectric parameters are given in Table II: the Seebeck coefficient S, power factor P, thermoelectric figure of merit ZT, and phonon thermal conductance κ_{ph}. The given ZT values are the maximum values near the conduction and valance band edges, and the Seebeck coefficient and the power factor values correspond to the chemical potentials where ZT is maximized.

For the sake of comparison, at 300 and 800 K, the width dependence of p- and n-type S, P, and ZT values of the structures are plotted in Fig. 6. As can be seen, p-type S values are higher than that of 2D $HfSe_2$ at both temperatures [see Fig. 6(a)]. At 300 K, p-type S is almost the same for each NR (except for $n = 6$ and $n = 14$), and its average value is 2.38×10^{-4} V K^{-1}. At 800 K, the effect of the symmetry difference on S reveals itself slightly. In Fig. 6(b), the absolute value of n-type S is given. The results of NRs with even and odd n are significantly different from each other at both temperatures. The n-type S is improved for the NRs with $n = 6, 8, 10, 13$ at 300 K and $n = 8$ at 800 K. The rest of the n-type S values are either closer to or less than that of 2D $HfSe_2$. The convergence to the 2D limit is seen merely for n-type S. Moreover, having bands with closer energy values increases the valley degeneracy [80,81], which causes dramatic changes in $\tau(\varepsilon)$; consequently, S increases [31]. This can be seen for the odd-numbered $HfSe_2$ NRs at 300 and 800 K. The n-type S has an increasing graph for NRs with odd n since the conduction band degeneracy increases with

TABLE II. The calculated parameters of 2D $HfSe_2$ and its NR structures are the Seebeck coefficient S, the power factor P, the thermoelectric figure of merit ZT, and the phonon thermal conductance κ_{ph}. The given values are p-type/n-type thermoelectric transport coefficients. Results for the 2D $HfSe_2$ structure are from Ref. [42].

	S ($\times 10^{-4}$ V K^{-1})		P ($\times 10^{-3}$ W K^{-2} m^{-2})		ZT		κ_{ph} (W K^{-1} m^{-1})	
	300 K	800 K	300 K	800 K	300 K	800 K	300 K	800 K
2D $HfSe_2$	1.92/−2.20	2.12/−2.65	0.56/1.84	0.92/2.61	0.26/0.75	0.84/2.11	0.59	0.61
$n = 15$	2.37/−2.25	2.54/−2.64	1.42/1.42	2.03/2.73	0.76/0.66	1.86/2.24	0.17	0.17
$n = 14$	2.11/−2.17	2.54/−2.68	1.33/1.52	1.85/2.61	0.77/0.88	1.90/2.21	0.18	0.19
$n = 13$	2.35/−2.36	2.47/−2.63	1.40/1.08	1.78/2.25	0.89/0.62	1.96/2.16	0.18	0.18
$n = 12$	2.39/−2.15	2.49/−2.65	1.32/1.48	1.66/1.96	0.83/0.95	1.97/2.11	0.18	0.18
$n = 11$	2.39/−2.24	2.45/−2.62	1.31/0.97	1.58/2.00	0.91/0.61	2.01/2.10	0.18	0.18
$n = 10$	2.38/−2.44	2.54/−2.70	1.31/1.47	1.50/1.72	0.94/1.07	2.15/2.27	0.18	0.19
$n = 9$	2.38/−2.20	2.52/−2.54	1.31/0.80	1.47/1.31	1.02/0.68	2.24/1.81	0.19	0.19
$n = 8$	2.37/−2.45	2.57/−2.83	1.12/1.47	1.38/1.75	0.95/1.27	2.43/2.69	0.21	0.21
$n = 7$	2.37/−2.22	2.55/−2.45	1.12/0.82	1.37/1.13	1.08/0.85	2.57/2.09	0.21	0.21
$n = 6$	2.25/−2.45	2.72/−2.68	0.83/1.47	1.24/1.38	0.94/1.55	2.62/3.12	0.21	0.22

n, and this results in the abrupt changes in their transmission spectra.

Structural symmetry does not cause a considerable difference in p-type P values at both temperatures. As seen in Fig. 6(c), the p-type P values of each NR are enhanced at 300 and 800 K. On the other hand, the n-type P values are below the 2D limit at both temperatures. At both temperatures, the n-type P values of NRs show a different trend due to the symmetry difference. Due to the band degeneracy, the P value increases with the increasing n. The band degeneracy not only boosts the transmission but also leads to abrupt changes in transmission. The latter case results in two closer peaks in P which overlap with increasing n, as seen in Fig. 7(a). This is why NRs with odd n have an increasing trend at 300 K. On the other hand, for the NRs with even n, the distance between the two peaks remains almost the same as n increases [see

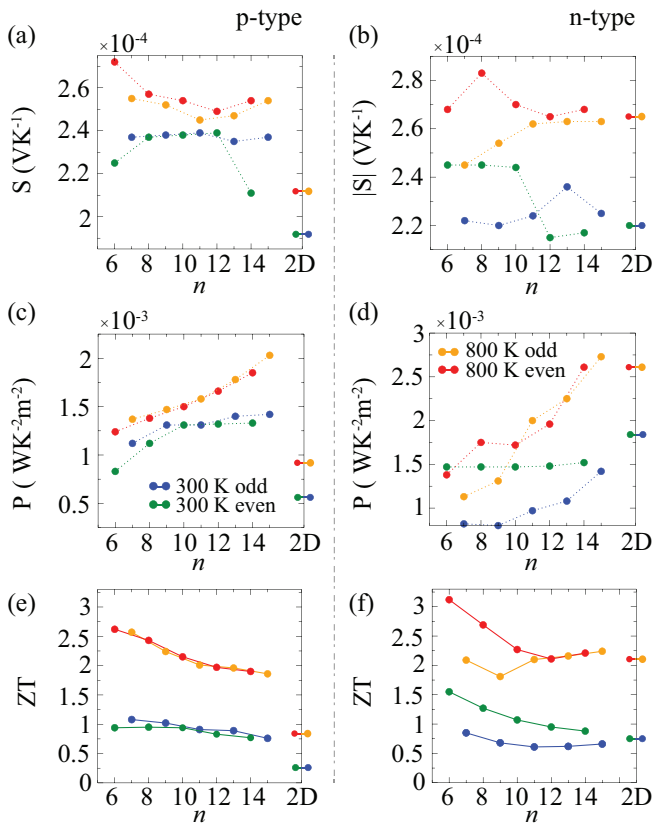

FIG. 6. The p-type (left) and (right) n-type Seebeck coefficient S, the power factor P, and the thermoelectric figure of merit ZT are given for the each NR. The absolute values are considered for the n-type Seebeck coefficient. The S, P, and ZT values of 2D $HfSe_2$ [42] are also shown in the graphs.

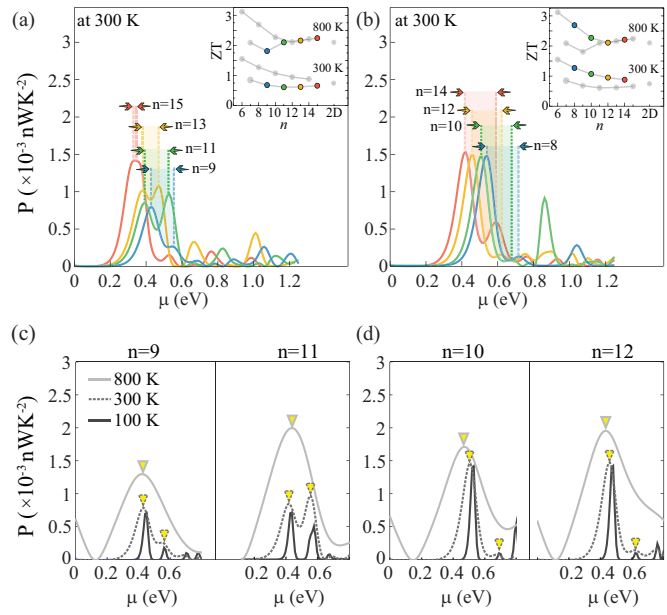

FIG. 7. At 300 K, the n-type power factor P values of the NRs with (a) odd and (b) even n are given as a function of chemical potential μ. In the insets, the thermoelectric figure of merit ZT is given as a reminder. For the NRs with (c) odd and (d) even n, overlapping in n-type P caused by temperature is shown. The peaks are indicated with yellow triangles.

Fig. 7(b)]. Therefore, at 300 K, NRs with even n have close n-type P values, on average 1.48×10^{-3} W K^{-2} m^{-2}, while NRs with odd n have an increasing trend. However, at 800 K, n-type P of each NR increase with increasing n. For both NRs with even and odd n, there are two peaks: a major peak (at the conduction band edge) and a secondary peak. The secondary peak in P contributes to the major one when the temperature is increased, and this results in an increase in P [see Figs. 7(c) and 7(d)]. For the structures with $n = 11, 13, 15$, these two peaks are close. For the rest of the NRs, the secondary peaks are much lower than the major ones. Therefore, the increase in n-type P values of the NRs with $n = 11, 13, 15$ is more than that of the others. In the ballistic regime, the transport properties are determined by the number of transport channels available, which means the geometry of the structure takes an important role. Reduction in the dimension of the material leads to a decrease in its lattice thermal conductivity due to the decreased number of transport channels. Therefore, when the width of the structure decreases, an increase in its ZT value is expected. This behavior is seen in Figs. 6(e) and 6(f) for the NRs, except for the odd-numbered structures at 800 K. In order to understand this, we examine their thermoelectric properties in detail. At various temperatures, the power factor and ZT graphs are shown in Fig. 7. The graphs of NRs with even n are shown in Fig. 7(b), and those with odd n are shown in Fig. 7(a). ZT of the structure with $n = 11$ and $n = 13$ have higher values than those of the narrower NRs. As seen in Fig. 4, as n increases, the first conduction plateau of the transmission spectrum is getting narrower due to the degeneracy in conduction bands. The abrupt changes in the transmission result in having two peaks with similar values in their power factor values. At low temperatures, these two peaks are separated from each other. As the temperature increases, these peaks overlap, and this causes an increase in the n-type ZT values of NRs with $n = 11$ and $n = 13$.

As seen in Fig. 6, the p-type ZT values of NRs with odd and even n are enhanced at both low and high temperatures, and the ZT values of NRs converge to the 2D limit with increasing width. In addition, the p-type ZT values does not depend on the symmetry of the structure since the structures with even and odd n have similar dispersions in their electronic structure [see Figs. 4(c) and 4(d); the dispersions of the valence bands are nearly the same]. There is no considerable increase in n-type ZT values of NRs with odd n at low temperatures. The n-type ZT values of NRs with even n decrease with n, and ZT is doubled when the n-type ZT of 2D $HfSe_2$ is compared with that of NR with $n = 6$ (see Table II). The n-type ZT values of even-n structures converge to the 2D limit as the NR gets wider.

At higher temperatures, the n-type ZT values of NRs with even n decrease with an expected trend as the structures get larger. The conduction plateaus of structures with even n are relatively wider than those of NRs with odd n. In other words, the NR structures with even n have no abrupt changes in their transmission function in the 0–1-eV energy range.

The calculated phonon thermal conductance κ_{ph} values are normalized with the NR widths. κ_{ph} values at 300 and 800 K are given in Table II, and the temperature dependency of the κ_{ph} is shown in Fig. 8. In 1D systems, κ_{ph} changes linearly with T at low temperatures. As seen from the inset in Fig. 8,

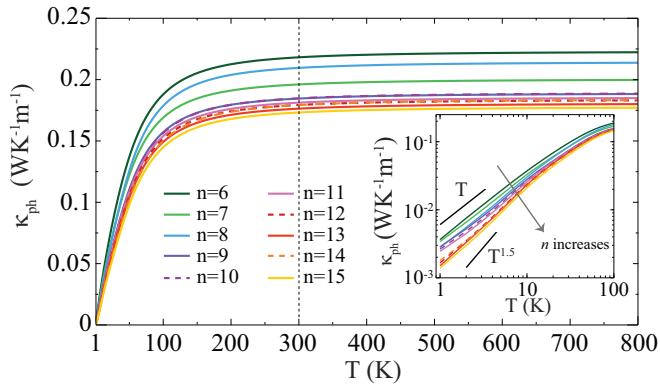

FIG. 8. The phonon thermal conductance κ_{ph} of the NR structures are given as a function of temperature T. The inset shows κ_{ph} on a logarithmic scale. At low temperatures, the κ_{ph} values of NRs have linear dependence on T.

for the NR with $n = 6$, κ_{ph} and T are linearly dependent on each other. With increasing width, converging to the 2D system, the form of the low-temperature dependence of the thermal conductance gets closer to $\kappa_{ph} \sim T^{1.5}$. Moreover, the nonscaled values of κ_{ph} for each NR are close to each other, and they are about one third of κ_{ph} of the 2D structure. It is known that the main contribution to κ_{ph} comes from the acoustic modes. When the κ_{ph} values are scaled with respect to the NR widths, the contribution from these modes becomes less for the wider NRs. Consequently, the κ_{ph} per width value increases with decreasing width. Since the acoustic modes are the low-frequency modes, this behavior is seen prominently at low temperatures. This behavior is also reported for the ballistic thermal conductance of graphene NRs [82]. Furthermore, the convergence of κ_{ph} to the 2D limit can be observed by constructing NRs with larger widths; however, this increases the computational cost.

To summarize, the phonon thermal conductance of T-$HfSe_2$ is reduced to one third via nanostructuring. It is found that mainly, the p-type thermoelectric coefficients are affected by the symmetry difference. The p-type Seebeck coefficient and power factor are enhanced, and the p-type ZT value approaches to the n-type values at both 300 and 800 K. The n-type ZT of 2D $HfSe_2$ has a relatively high value; therefore, there is no improvement in n-type ZT at either low or high temperatures.

IV. CONCLUSIONS

In this study, we investigated the physical properties of armchair nanoribbons of the 2D trigonal phase of $HfSe_2$. We examined the ballistic transport properties within the Landauer formalism with a combination of DFT-based *ab initio* calculations. The NRs have two different edge symmetries which depend on the number of atoms n within their widths. Their vibrational band spectra show the dynamically stability of each NR structure. The NR structures have a semiconducting character, and their electronic band gap values vary between the infrared and visible regions. As the structure gets narrower, its band gap value is shifted toward the visible region. The structural symmetry difference

in $HfSe_2$ NRs reveals itself in the electronic band structure. The even- and odd-numbered NRs have different electronic band dispersions. Conduction band degeneracy and the band convergence in valence bands are observed with the reduction in the dimension of the $HfSe_2$ crystal. Herein, the phonon thermal conductance was reduced to one third of T-$HfSe_2$ via nanostructuring. We achieved improving the p-type Seebeck coefficient and the power factor for the T-phase $HfSe_2$ at both 300 and 800 K. Our results show that the p-type ZT values are doubled at both low and high temperatures, and at these temperatures the p-type ZT value is approximated to the n-type ZT values. At both 300 and 800 K, the n-type ZT is relatively high for the 2D $HfSe_2$ structure, and its value cannot be improved via nanostructuring. The n-type ZT values of NRs with odd n do not change significantly at 300 K, and they show an unexpected behavior at 800 K due to the degenerate conduction bands.

ACKNOWLEDGMENTS

The authors offer many thanks to G. Özbal Sargın for her fruitful discussions and suggestions throughout this study. Computational resources were provided by the Scientific and Technological Research Council of Turkey (TÜBİTAK). The authors acknowledge financial support from the TÜBİTAK through projects funded by Grants No. 117F131 and No. 117F480.

[1] X. Zhang and L.-D. Zhao, J. Materiomics **1**, 92 (2015).
[2] S. Riffat and X. Ma, Appl. Therm. Eng. **23**, 913 (2003).
[3] G. J. Snyder and A. H. Snyder, Energy Environ. Sci. **10**, 2280 (2017).
[4] D. Champier, in *3rd International Congress on Energy Efficiency and Energy Related Materials (ENEFM2015): Proceedings, Oludeniz, Turkey, 19–23 October 2015* (Springer International Publishing AG, Cham, Switzerland, 2017), pp. 203–212.
[5] F. K. Shaikh and S. Zeadally, Renew. Sustain. Energy Rev. **55**, 1041 (2016).
[6] G. D. Mahan and J. O. Sofo, Proc. Natl. Acad. Sci. USA **93**, 7436 (1996).
[7] X. Chen, Y. Wang, T. Cui, Y. Ma, G. Zou, and T. Iitaka, J. Chem. Phys. **128**, 194713 (2008).
[8] M. V. Lukowicz, E. Abbe, T. Schmiel, and M. Tajmar, Energies **9**, 541 (2016).
[9] J.-c. Zheng, Front. Phys. China **3**, 269 (2008).
[10] B. Poudel, Q. Hao, Y. Ma, Y. Lan, A. Minnich, B. Yu, X. Yan, D. Wang, A. Muto, D. Vashaee, X. Chen, J. Liu, M. S. Dresselhaus, G. Chen, and Z. Ren, Science **320**, 634 (2008).
[11] J. Mao, H. Zhu, Z. Ding, Z. Liu, G. A. Gamage, G. Chen, and Z. Ren, Science **365**, 495 (2019).
[12] Y. Xiao and L. Zhao, npj Quantum Mater. **3**, 55 (2018).
[13] R. Franz and G. Wiedemann, Ann. Phys. (Berlin, Ger.) **165**, 497 (1853).
[14] G. A. Slack, Solid State Phys. **34**, 376 (1979).
[15] G. A. Slack, *CRC Handbook of Thermoelectrics*, edited by D. Rowe (CRC Press, Boca Raton, FL, 1995).
[16] G. Snyder and E. Toberer, Nat. Mater. **7**, 105 (2008).
[17] M. Beekman, D. Morelli, and G. Nolas, Nat. Mater. **14**, 1182 (2015).
[18] A. A. Balandin, Nat. Mater. **10**, 569 (2011).
[19] H. Alam and S. Ramakrishna, Nano Energy **2**, 190 (2013).
[20] T. M. Wu, R. X. Xu, X. Zheng, and W. Zhuang, Chin. J Chem. Phys. **29**, 445 (2016).
[21] L. D. Hicks and M. S. Dresselhaus, Phys. Rev. B **47**, 12727 (1993).
[22] L. D. Hicks and M. S. Dresselhaus, Phys. Rev. B **47**, 16631 (1993).
[23] P. Pichanusakorn and P. Bandaru, Mater. Sci. Eng. R **67**, 19 (2010).
[24] G. D. Guttman, E. Ben-Jacob, and D. J. Bergman, Phys. Rev. B **51**, 17758 (1995).
[25] T. Gunst, T. Markussen, A.-P. Jauho, and M. Brandbyge, Phys. Rev. B **84**, 155449 (2011).
[26] M. Dresselhaus, G. Chen, M. Tang, R. Yang, H. Lee, D. Wang, Z. Ren, J. Fleurial, and P. Gogna, Adv. Mater. **19**, 1043 (2007).
[27] L. D. Hicks, T. C. Harman, X. Sun, and M. S. Dresselhaus, Phys. Rev. B **53**, R10493 (1996).
[28] D. A. Broido and T. L. Reinecke, Appl. Phys. Lett. **67**, 100 (1995).
[29] C. Rudderham and J. Maassen, J. Appl. Phys. **127**, 065105 (2020).
[30] R. Kim, S. Datta, and M. S. Lundstrom, J. Appl. Phys. **105**, 034506 (2009).
[31] M. Cutler and N. F. Mott, Phys. Rev. **181**, 1336 (1969).
[32] L. Friedman, J. Phys. C **17**, 3999 (1984).
[33] A. H. Wilson, *Theory of Metals*, 2nd ed. (Cambridge University Press, Cambridge, 1958), p. 204.
[34] A. H. Wilson, *Inorganic Two-Dimensional Nanomterials: Fundamental Understanding, Characterization, and Energy Applications*, edited by C. Wu (Royal Society of Chemistry, Cambridge, UK, 2017), pp. 386–388.
[35] X. Zhang, D. Sun, Y. Li, G.-H. Lee, X. Cui, D. Chenet, Y. You, T. F. Heinz, and J. C. Hone, ACS Appl. Mater. Interfaces **7**, 25923 (2015).
[36] S. Sahoo, A. P. S. Gaur, M. Ahmadi, M. J.-F. Guinel, and R. S. Katiyar, J. Phys. Chem. C **117**, 9042 (2013).
[37] Y.-X. Zhen, M. Yang, H. Zhang, G.-S. Fu, J.-L. Wang, S.-F.Wang, and R.-N. Wang, Sci. Bull. **62**, 1530 (2017).
[38] J. Hong, C. Lee, J.-S. Park, and J. H. Shim, Phys. Rev. B **93**, 035445 (2016).
[39] G. Zhang and Y.-W. Zhang, J. Mater. Chem. C **5**, 7684 (2017).
[40] D. B. Velusamy, R. H. Kim, S. Cha, J. Huh, R. Khazaeinezhad, S. H. Kassani, G. Song, S. M. Cho, S. H. Cho, I. Hwang, J. Lee, K. Oh, H. Choi, and C. Park, Nat. Commun. **6**, 8063 (2015).
[41] A. Castellanos-Gomez, M. Poot, G. A. Steele, H. S. J. van der Zant, N. Agraït, and G. Rubio-Bollinger, Adv. Mater. **24**, 772 (2012).
[42] G. Özbal, R. T. Senger, C. Sevik, and H. Sevinçli, Phys. Rev. B **100**, 085415 (2019).
[43] S.-D. Guo and Y.-H. Wang, J. Appl. Phys. **121**, 034302 (2017).

[44] C. Yan, C. Gong, P. Wangyang, J. Chu, K. Hu, C. Li, X. Wang, X. Du, T. Zhai, Y. Li, and J. Xiong, Adv. Funct. Mater. **28**, 1803305 (2018).

[45] G. Yumnam, T. Pandey, and A. K. Singh, J. Chem. Phys. **143**, 234704 (2015).

[46] M. K. Mohanta, A. Rawat, N. Jena, R. Ahammed, and A. D. Sarkar, J. Phys. Condens. Matter **32**, 355301 (2020).

[47] G. Ding, G. Y. Gao, Z. Huang, W. Zhang, and K. Yao, Nanotechnology **27**, 375703 (2016).

[48] M. J. Mleczko, C. Zhang, H. R. Lee, H. H. Kuo, B. Magyari-Kope, R. G. Moore, Z. X. Shen, I. R. Fisher, Y. Nishi, and E. Pop, Sci. Adv. **3**, e1700481 (2017).

[49] G. Kresse and J. Hafner, Phys. Rev. B **47**, 558 (1993).

[50] G. Kresse and J. Hafner, Phys. Rev. B **49**, 14251 (1994).

[51] J. P. Perdew, K. Burke, and M. Ernzerhof, Phys. Rev. Lett. **77**, 3865 (1996).

[52] A. V. Krukau, G. E. Scuseria, J. P. Perdew, and A. Savin, J. Chem. Phys. **129**, 124103 (2008).

[53] A. Togo and I. Tanaka, Scr. Mater. **108**, 1 (2015).

[54] R. Landauer, Philos. Mag. **21**, 863 (1970).

[55] M. Büttiker, Phys. Rev. Lett. **57**, 1761 (1986).

[56] S. Datta, Phys. Rev. B **45**, 1347 (1992).

[57] L. F. Torres, S. Roche, and J.-C. Charlier, *Introduction to Graphene-Based Nanomaterials from Electronic Structure to Quantum Transport* (Cambridge University Press, Cambridge, 2014), pp. 91–117.

[58] D. A. Ryndyk, *Theory of Quantum Transport at Nanoscale: An Introduction* (Springer, Switzerland, 2016), pp. 1–10.

[59] M. Dragoman and D. Dragoman, *2D Nanoelectronics: Physics and Devices of Atomically Thin Materials* (Springer, Switzerland, 2017).

[60] J. Chang, L. F. Register, and S. K. Banerjee, *2013 International Conference on Simulation of Semiconductor Processes and Devices (SISPAD)* (IEEE, Piscataway, NJ, 2013), pp. 408–411.

[61] M. Konôpka and P. Dieška, Phys. E (Amsterdam, Neth.) **97**, 259 (2018).

[62] J. Baringhaus, M. Ruan, F. Edler *et al.*, Nature (London) **506**, 349 (2014).

[63] C. White and T. Todorov, Nature (London) **393**, 240 (1998).

[64] L. Wang, I. Meric, P. Y. Huang, Q. Gao, Y. Gao, H. Tran, T. Taniguchi, K. Watanabe, L. M. Campos, D. A. Muller, J. Guo, P. Kim, J. Hone, K. L. Shepard, and C. R. Dean, Science **342**, 614 (2013).

[65] F. Zhang, Ph.D. thesis, Columbia University, 2017.

[66] J. Ma, W. Li, and X. Luo, Appl. Phys. Lett. **108**, 082102 (2016).

[67] F. Pizzocchero, L. Gammelgaard, B. S. Jessen, J. M. Caridad, L. Wang, J. Hone, P. Bøggild, and T. J. Booth, Nat. Commun. **7**, 11894 (2016).

[68] J. Bardeen and W. Shockley, Phys. Rev. **80**, 72 (1950).

[69] J. Xi, M. Long, L. Tang, D. Wang, and Z. Shuai, Nanoscale **4**, 4348 (2012).

[70] U. Sivan and Y. Imry, Phys. Rev. B **33**, 551 (1986).

[71] K. Esfarjani, M. Zebarjadi, and Y. Kawazoe, Phys. Rev. B **73**, 085406 (2006).

[72] L. G. C. Rego and G. Kirczenow, Phys. Rev. Lett. **81**, 232 (1998).

[73] H. Sevinçli, S. Roche, G. Cuniberti, M. Brandbyge, R. Gutierrez, and L. M. Sandonas, J. Phys.: Condens. Matter. **31**, 273003 (2019).

[74] R. Saito, G. Dresselhaus, and M. S. Dresselhaus, *Physical Properties of Carbon Nanotubes* (Imperial College Press, London, 1998).

[75] X. Liu, J. Gao, G. Zhang, and Y.-W. Zhang, Adv. Funct. Mater. **27**, 1702776 (2017).

[76] R. Gillen, M. Mohr, C. Thomsen, and J. Maultzsch, Phys. Rev. B **80**, 155418 (2009).

[77] R. Gillen, M. Mohr, and J. Maultzsch, Phys. Rev. B **81**, 205426 (2010).

[78] K. Nakada, M. Fujita, G. Dresselhaus, and M. S. Dresselhaus, Phys. Rev. B **54**, 17954 (1996).

[79] G. D. Mahan, *Solid State Physics, Vol. 51* (Academic Press, San Diego, 1998), p. 84.

[80] Y. Pei, H. Wang, and G. J. Snyder, Adv. Mater. **24**, 6125 (2012).

[81] H. J. Goldsmid, *Thermoelectric Refrigeration* (Springer, Berlin, Heidelberg, 1964).

[82] H. Tomita and J. Nakamura, J. Vac. Sci. Technol. B **31**, 04D104-1 (2013).